

Submitted for Publication, July 1996

Thin Saline Ice Thickness Retrieval Using Time Series C-Band Polarimetric Radar Measurements

**S. E. Shih, K. H. Ding, S. V. Nghiem†
C. C. Hsu, J. A. Kong, and A. K. Jordan†**

**1 Department of Electrical Engineering and Computer Science
and Research Laboratory of Electronics
Massachusetts Institute of Technology
Cambridge, Massachusetts**

**† Center for Space Microelectronics Technology
Jet Propulsion Laboratory
California Institute of Technology
Pasadena, California**

**† Remote Sensing Division
Naval Research Laboratory
Washington, DC**

**Mailing address : Dr. S. V. Nghiem, Jet Propulsion Laboratory
Mail Stop 300-235, 4800 Oak Grove Drive, Pasadena, CA 91109**

Thin Saline Ice Thickness Retrieval Using Time Series C-Band Polarimetric Radar Measurements

S.B. Shih, K.H. Ding, S.V. Nghiem[‡], C.C. Hsu, J.A. Kong, and A.K. Jordan[‡]

Department of Electrical Engineering and Computer Science
and Research Laboratory of Electronics
Massachusetts Institute of Technology, Cambridge, MA 02139

[‡] Center for Space Microelectronics Technology

Jet Propulsion Laboratory

California Institute of Technology, Pasadena, CA 91109

[‡] Remote Sensing Division

Naval Research Laboratory, Washington, DC 20375

Abstract

The application of time-series radar measurements to accurately invert the thickness of saline ice is presented in this study. We describe briefly some experimental observations from the CRRMEX 93 campaign of sea ice. It indicates that the volume scattering of brine inclusions is an important contribution to the backscatter response of saline ice. From the experimental findings and the thermophysics of ice growth, we develop an inversion algorithm for the ice thickness based on a dynamic-electromagnetic scattering model of saline ice. This inversion algorithm uses a parametric estimation approach where the radiative transfer equation is used as the direct scattering model to calculate the backscattering signatures from ice medium, and the Levenberg-Marquardt method is employed to retrieve ice thickness iteratively. Additional information provided by the saline ice thermodynamics is applied to constrain the electromagnetic inverse problem to achieve a more accurate reconstruction. The inversion results using this algorithm and the data from CRRMEX 93 experiment are presented. The demonstrated accurate thickness retrieval suggests the potential usage of this algorithm for satellite remote sensing of sea ice.

1. INTRODUCTION

The large coverage of sea ice in polar regions has a great impact on the Earth's climate system [1]. The thickness of sea ice is an important factor in understanding the dynamics of sea ice cover and the heat exchange between the ocean and the atmosphere. In particular, the winter flux of oceanic heat to the atmosphere through the thin ice cover can be two orders of magnitude greater than from the adjacent areas of thick ice [2]. Therefore, information about thin sea ice is essential, at least regionally, to the heat budget balance. Although the spaceborne synthetic aperture radar (SAR) images has been successfully applied in mapping the extent and identifying the types of sea ice [3], it still remains a rudimentary issue for direct determination of sea ice thickness from space. This is particularly important in view of the present European Remote Sensing Satellite (ERS) and Canadian RADARSAT which have been orbited in monitoring the polar regions [4, 5]. Recently, some work has been done using airborne radar measurements to retrieve sea ice thickness. For example, Kwok *et al.* [6] have applied the neural network approach to estimate the ice thickness distribution using multiple-frequency polarimetric SAR data, and Winebrenner *et al.* [7] have studied refreezing leads from a single frequency polarimetric SAR data with a radar signature model based on the rough air-ice interface scattering.

In general, the dynamic environmental conditions and the susceptible ice physical and morphological characteristics complicate the interactions of electromagnetic waves with the sea ice medium. As a result, the direct usage of a simple empirical model for sea ice thickness retrieval becomes limited. In the past two decades, several sea ice direct scattering models have been developed and verified by various experiments [8- 12]. Usually these models are complicated and are difficult to find closed-form solutions for direct inversion. To utilize these developed scattering models for ice thickness retrieval, the parametric estimation method offers a greater flexibility in the choice of direct scattering models, the parameters to be inverted, and the data to be employed [1- 3]. However, such an approach usually comes with the problems of non-unique solutions and inversion stability with noisy data. Although it is possible to reduce the effects of these uncertainties by using diversified data like multi-frequency, multi-angle, and polarimetric data, the cost of such extensive measurements may be prohibitive for satellite remote sensing of sea ice. On the other hand, orbited satellites repeat their passes at a fixed time interval; it is natural for them to make time-series observations. With these measurements, more data become available which may be helpful for resolving the non-uniqueness and stability problems, and useful for the geophysical parameter reconstruction.

The use of time-series data in the inverse scattering problem has been theoretically investigated by Veysoglu *et al.* [14, 15] with applications to the passive microwave remote sensing of sea ice. Their studies have demonstrated that, by incorporating a Stefan's growth model

[16] into the inversion algorithm, the thickness estimation can be constrained sufficiently to predict more accurately the evolution of sea ice growth using passive microwave measurements. In what follows we develop a thickness retrieval algorithm based on a dynamic-electromagnetic scattering model of saline ice and the time-series active remote sensing data. This inversion algorithm is then applied to reconstruct the growth of a sheet of thin saline ice by using C-band polarimetric radar sequential measurements from CRREL/LEX 93 experiment. This experiment was conducted at the U. S. Army Cold Regions Research and Engineering Laboratory (CRREL) in September 1993. The experimental findings are briefly described in Section 11, and details are referred to Nghiem *et al.* [17]. In Section III, a dynamic-electromagnetic scattering model of saline ice is developed. This direct scattering model consists of a saline ice physical model describing the dynamic variation of ice characteristics coupled with an electromagnetic scattering model accounting for wave propagation and scattering in random medium. Interpretations of experimental are also demonstrated here. The inversion algorithm using time-series data based on this direct scattering model and a parametric estimation approach is described in Section IV. The inversion results for saline ice thickness retrieval and comparisons with ground truth are given in Section V. The advantage of using time-series data for the inversion is also discussed in this section. The summary is presented in Section VI.

11. DESCRIPTION OF SALINE ICE GROWTH EXPERIMENT

In order to investigate the electromagnetic scattering mechanisms involved in thin sea ice, to relate polarimetric backscatter signatures to ice physical characteristics, and to assess the feasibility of thickness inversion, a saline ice experiment was conducted by the Jet Propulsion Laboratory (JPL) and the Massachusetts Institute of Technology (MIT), in conjunction with the U. S. Army Cold Regions Research and Engineering Laboratory (CRREL). This saline ice growth experiment in an indoor refrigerated facility was carried out during September 1993 at CRREL in Hanover, New Hampshire. In this section the evolution of measured C-band polarimetric backscatter signatures and physical characteristics of saline ice during its growth are briefly described and discussed. The detailed experimental set up, procedures, and findings have been reported by Nghiem *et al.* [17].

In the experiment, the ice sheet was grown from open saline water with a salinity of 32 ‰ under quiescent conditions. The air and water temperatures were kept constantly at about -21.8°C and -2.0°C , respectively, to mimic the Arctic sea ice growth conditions. During the ice growth, a C-band polarimetric scatterometer was used to collect backscatter data at various incident angles. The measurements were made at an interval about every centimeter of ice growth up to 11.2 cm in ice thickness. At the same time, ice samples were taken from the pond to characterize their physical properties such as thickness, temperature,

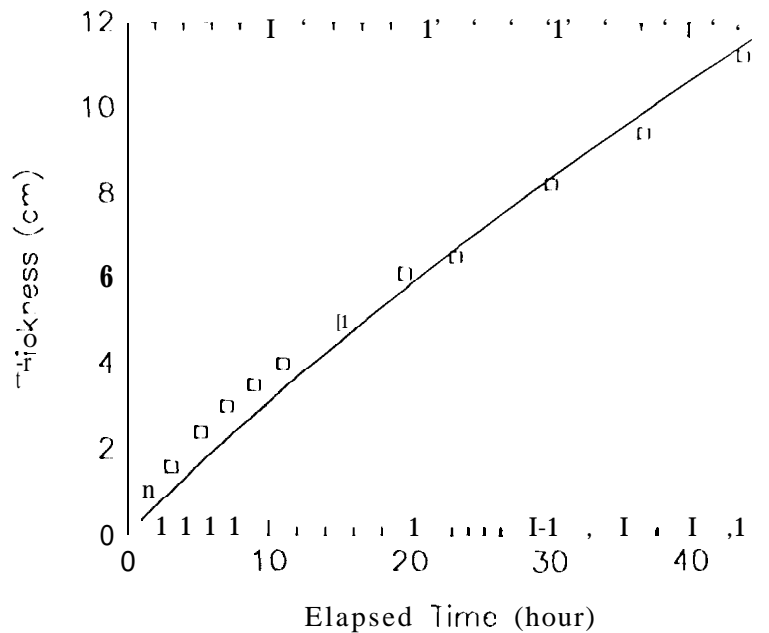


Figure 1 : CR DELLEX'93 thin ice growth. [] represents measured ice thickness. Solid line is the simulation of ice growth using thermodynamic model

and salinity. The evolution of ice thickness during the two-day growth is shown in Figure 1. The growth rate is about 0.23 cm/hr. The symbol represents measured thickness and the continuous curve is obtained from an ice growth simulation which will be described in the next section. Increasing ice thickness is accompanied by the desalination of ice sheet. Figure 2 reveals a roughly 30% reduction in the bulk salinity S_i (‰) as a function of thickness h (cm). The experimental data have been fitted by a linear curve with a correlation coefficient about 0.90,

$$S_i = 16.0 - 0.532h \quad (1)$$

for $1 \text{ cm} < h < 10 \text{ cm}$. The desalination may clue mainly to the processes of brine migration and gravity drainage under the controlled laboratory conditions [1-7]. Both the thickness growth and the desalination rates of saline ice are compared quite well with those from sea ice experiments [18,19].

Measured polarimetric backscattering coefficients are shown in Figures 3 and 4 for 25° and 30° incident angles, respectively. It is noted that there is a large increase of 8-10 dB for all three polarizations (VV, HH, and HV) as ice grows from 3 cm to 11.2 cm. Although the backscatter from sea ice may be caused by several possible mechanisms including the surface scattering from both air-ice and ice-water interface roughness, and scattering from brine inclusions within the ice sheet. However, the large increase of backscatter is hard to be explained by the commonly used surface scattering models, since the air-ice interface is measured very smooth and unchanged during the experiment and the ice-water interface

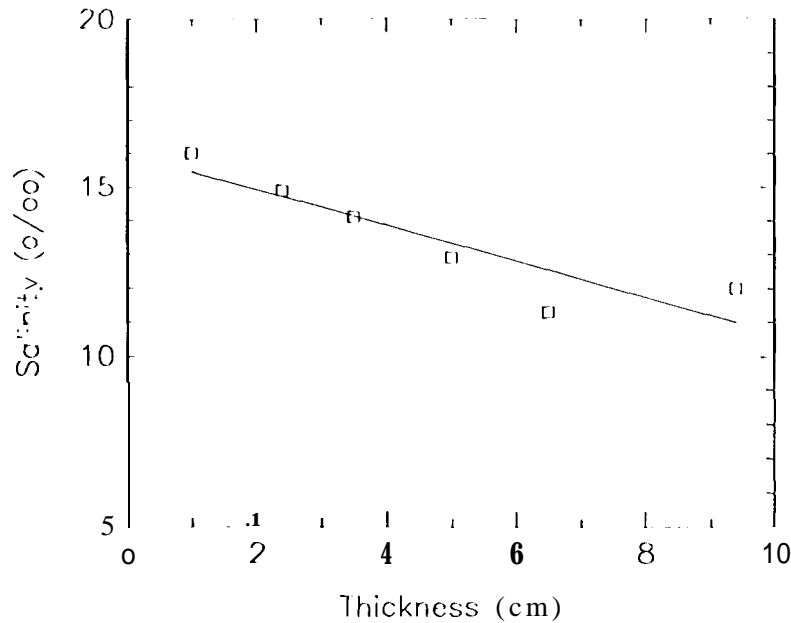


Figure 2: CRRELEX'93 saline ice bulk salinity. [1] represents the measured salinity data. Solid line is the linear fit of these data.

under the lossy ice layer has a dendritic structure with a relatively constant brine layer spacing [17]. This suggests that volume scattering from brine inclusions may be the dominant contribution for this large backscatter increase. Nevertheless, in view of volume scattering, without including the absorption and scattering loss, a four times increase of ice thickness can only account for at most 6 dB increase, and the losses will further decrease this value. Thus, thickness only can not explain this experimental observation, some other dynamic processes have to be considered. As we know, the scattering from Rayleigh scatterers, in our case the brine inclusions are much smaller than the wavelength, is proportional to the sixth power of particle size. Therefore, the increase of size can contribute a lot to the backscatter. Plausible explanations for brine size changing with ice growth are side-wall melting in brine features and brine interconnections [17]. Both the dynamic desalination and size varying will be considered in the discussion of saline ice scattering model in the next section.

11. DYNAMIC-ELECTROMAGNETIC SCATTERING MODEL

For remote sensing of geophysical media, a physically-based electromagnetic scattering model not only provides insights into the important scattering mechanisms but also renders a useful tool in analyzing measurements and retrieving physical parameters. Geometric structures of earth terrain are generally very complex and electromagnetic wave interactions with geophysical media are further complicated by their time-varying physical properties. As

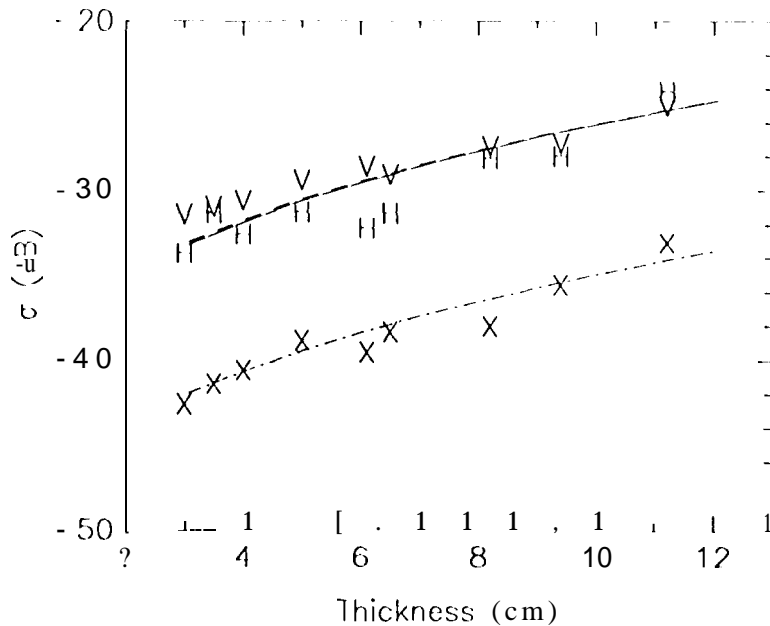


Figure 3: CRREL'93 measured backscatter and the simulation of backscattering coefficients from the radiative transfer equation. Incident angle is 25° . V, H, and X stand for measured data in VV polarization, HH polarization, and HV polarization, respectively. The corresponding simulation results are represented by solid line, dashed line, and dot-dashed line, respectively.

an example, sea ice characteristics, such as thickness, salinity, and brine size, are dynamic with its growth. These ice properties strongly affect radar signatures of sea ice. In this section, a saline ice physical model describing the dynamics of ice characteristics coupled with an electromagnetic scattering model accounting for the wave propagation and scattering is developed. This dynamic-electromagnetic scattering model is employed to interpret the evolution of thickness and polarimetric signatures during ice growth and is applied in the inversion algorithm to retrieve ice thickness in the later section.

A. Electromagnetic Scattering Model

Various electromagnetic scattering models of sea ice have been developed and applied in the study of sea ice remote sensing [8-12]. In accordance with the laboratory observations described in Section II, complexities in the ice structure such as rough interfaces and snow cover are ignored here. A layered scattering medium of saline ice with flat interfaces is considered here and the model configuration is depicted in Figure 5. The uppermost medium is air with permittivity ϵ_0 , the layer of thickness h represents the saline ice and the lower half space is saline water with complex permittivity ϵ_2 . Within the ice layer, the background is pure ice with complex permittivity ϵ_1 , brine inclusions are modeled as randomly distributed

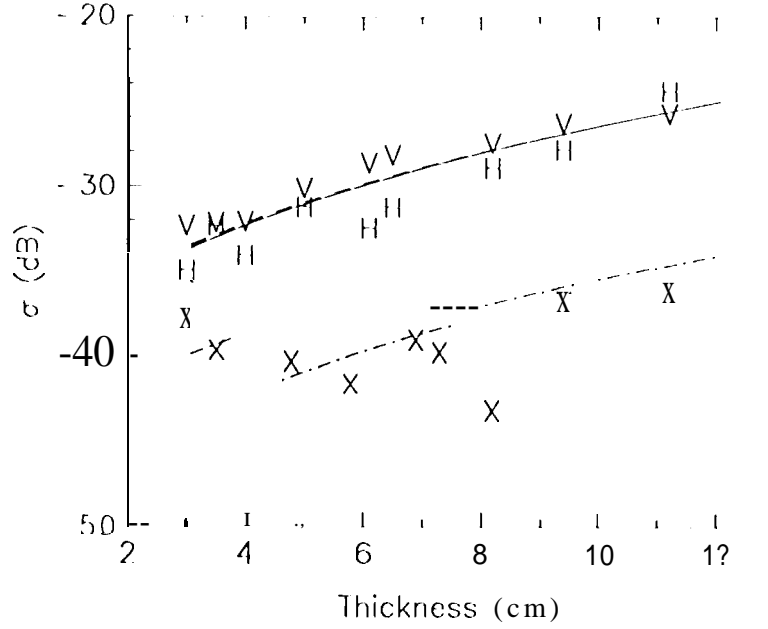


Figure 4: CRREL JEX'93 measured backscatter and the simulation of backscattering coefficients from the radiative transfer equation. Incident angle is 30° . V, H, and X stand for measured data in VV polarization, HH polarization, and HV polarization, respectively. The corresponding simulation results are represented by solid line, dashed line, and dot-dashed line, respectively.

but vertically oriented spheroids with complex permittivity ϵ_s . The three semi-axes of the particle are denoted as a , b , and c with $b = c$. The total fractional volume of brine pockets is f_v . The model parameters are subject to the dynamic changes of ice physical characteristics during the growth process.

With the configuration described above, the radiative transfer equation is applied to describe wave propagation and scattering through an ice layer [9],

$$\cos \theta \frac{d\bar{I}(\theta, \phi, z)}{dz} = -\bar{\kappa}_e(\theta, \phi) \cdot \bar{I}(\theta, \phi, z) + \int_{4\pi} d\Omega' \bar{P}(\theta, \phi; \theta', \phi') \cdot \bar{I}(\theta', \phi', z) \quad (2)$$

where $0 \leq \theta \leq \pi$ and $0 \leq \phi \leq 2\pi$. The quantity \bar{I} represents the Stokes vector, $\bar{\kappa}_e$ is the extinction matrix which includes both scattering and absorption losses, and $\bar{P}(\theta, \phi; \theta', \phi')$ denotes the phase matrix which describes how particles scatter radiation from the direction (θ', ϕ') into the direction (θ, ϕ) . Given boundary conditions, the specific intensity \bar{I} is solved using the iterative or the discrete eigen-analysis techniques [9]. In this study, a first-order iterative solution of radiative transfer equation (2) is used to calculate the electromagnetic scattering from saline ice. The explicit solution form is given as

$$\bar{I}_{0s}^{(1)}(\theta_0, \phi_0) = \bar{T}_{10}(\theta) \cdot \left[\bar{I} + \bar{M}(\theta, \phi) \cdot \bar{P}(\theta, \phi) \cdot \bar{R}_{12}(\theta) \cdot \bar{N}(\theta, \phi) \cdot \bar{R}_{10}(\theta) \right]$$

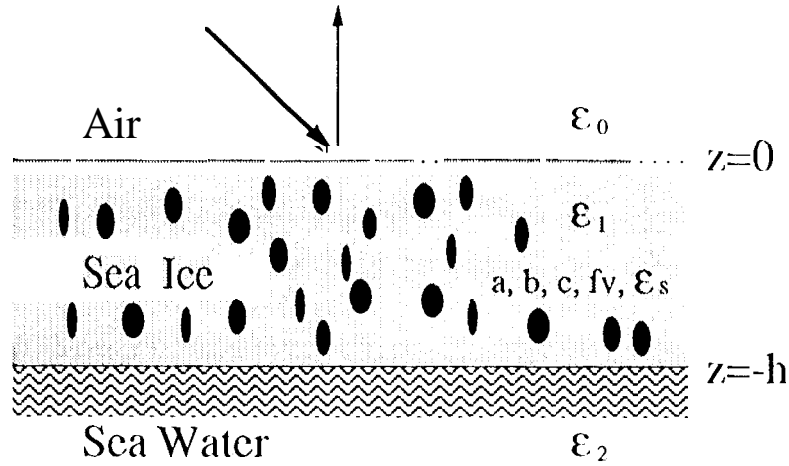


Figure 5: Electromagnetic scattering model of sea ice.

$$\begin{aligned}
 & \cdot [\bar{S}_1(\theta, \phi) - 1 \quad 32(0,4)] \\
 & + \bar{T}_{10}(\theta) \cdot [\bar{M}(\theta, \phi) \cdot \bar{P}(\theta, \phi) \cdot \bar{R}_{12}(\theta)] \\
 & \cdot [\bar{S}_3(\pi - \theta, \phi) \quad -; \bar{S}_4(\pi - \theta, \phi)]
 \end{aligned} \tag{3}$$

where (θ_0, ϕ_0) denotes the observation direction in the region 0, and (θ, ϕ) is the scattering direction inside the sea ice layer (region 1). Incident angle θ_0 is related to θ by Snell's law and ϕ_0 is equal to ϕ . \bar{T}_{0s} is the observed Stokes vector, \bar{I} is the identity matrix, and \bar{T}_{ij} and \bar{R}_{ij} are the respective transmission and reflection matrices for the boundary between regions i and j [9]. The four terms $\bar{S}_1(\theta, \phi)$, $\bar{S}_2(\theta, \phi)$, $\bar{S}_3(\pi - \theta, \phi)$, and $\bar{S}_4(\pi - \theta, \phi)$ describe four major volume and surface interactions: a single upward scattering by the particle, a reflection by the boundary at $z = -h$ and followed by a single upward scattering by the particle, a single downward scattering by the particle and then followed by a reflection off the boundary at $z = -h$, and a reflection by the boundary at $z = -h$, followed by a single downward scattering by the particles and further followed by a reflection off the boundary at $z = -h$, respectively [9]. Matrices $\bar{P}(\theta, \phi)$, $\bar{M}(\theta, \phi)$, and $\bar{N}(\theta, \phi)$ are related to the zeroth-order scattering solution which accounts for scattering and absorption losses at the specular direction. Detailed expressions for these matrices are given in the Appendix. The backscattering coefficient is calculated as

$$\sigma_{\beta\alpha}(\theta_{0i}) = 4\pi \cos \theta_{0i} \frac{I_{0s\beta}^{(1)}(\theta_{0i}, \phi_{0i} + \pi)}{I_{0i\alpha}(\pi - \theta_{0i}, \phi_{0i})} \tag{4}$$

where α, β can be v for vertical or h for horizontal polarization, and the subscripts i and s denote the incident and scattered waves, respectively.

B. Thin Saline Ice Growth Model

The formation and growth of sea ice is a complex process. In general, the ice growth rate is influenced by various environmental elements such as the air-sea temperature difference, wind, humidity, snow, sea current, and oceanic heat flux [20-22]. However, it is possible to obtain a reasonable estimation of ice growth by using a heat and mass balance equation [23,24]

$$\frac{dh}{dt} = \frac{1}{\rho L} \left[\frac{T_m - T_a}{h} + \frac{c}{k_i} \right] \quad (5)$$

where h is the ice thickness, $\frac{dh}{dt}$ is the growth rate, T_a is the air temperature, and T_m is the ice melting temperature. The thermal conductivity of saline ice k_i in $W/m/^\circ C$ can be calculated from an empirical formulation given by Maykut [20]

$$k_i = 9.828e^{-0.0057(T_i + 273)} + \frac{\beta S_i}{T_i} \quad (6)$$

where S_i is the bulk salinity in ‰, T_i is the ice temperature in $^\circ C$, and the constant $\beta = 0.13 W/m/(^\circ/100)$. It is noted that T_i can not be $0^\circ C$ unless S_i approaches zero [20]. L is the latent heat of freezing in J/kg ; an approximate expression for L has been obtained by Fukusako as [25],

$$L = 4.187 \times 10^3 \left(9.68 - 0.505T_m - 0.0273S_i + 4.3115 \frac{S_i}{T_m} + 8 \times 10^{-4} T_m S_i - 0.009T_m^2 \right) \quad (7)$$

where T_m is in $^\circ C$. The quantity c in (5) is the heat transfer coefficient between ice and air which accounts for contributions from both convection and radiation. A typical value of c is $11.6 W/m^2/^\circ C$ at $-40^\circ C$ under the still air condition [23]. ρ is the density of the ice. The density of gas-free saline ice can be related to temperature and salinity through the following equation [26]

$$\rho = \frac{\rho_i P_1(T_i)}{P_1(T_i) + \rho_i S_i P_2(T_i)} \quad (8)$$

where ρ_i is the pure ice density, and the functional forms of P_1 and P_2 can be found from the work of Cox and Weeks [26].

The growth process of sea ice also accompanies the desalination process. As the ice thickness increases, there is a continuous decrease in the ice salinity by mechanisms such as brine migration and gravity drainage. From the experimental observations presented in the previous section, the bulk salinity of thin saline ice is approximated by a monotonic decreasing function of ice layer thickness h and a desalination factor d_s as

$$S_i = S_{i0} - d_s h \quad (9)$$

for $1\text{ cm} < h < 10\text{ cm}$. It is plausible that, in the desalination process the drainage mechanism causes one brine to combine or interconnect with another one to form a larger brine feature [14]. Moreover, the temperature gradient between the brine and the surrounding ice background gives rise to the side-wall melting. Thus, a further assumption is made here of a linear increase of the brine inclusion size a with the thickness h and a size expansion factor g_s as

$$a = a_0 + g_s h \quad (10)$$

with $1\text{ cm} < h < 10\text{ cm}$. The difficulty is that there are no quantitative in situ measurements, to the best of our knowledge, on how the brine size changes with the growth of ice. However, the assumption made here will be tested by comparing the theoretical results with the experimental data on radar backscatter signatures.

C. Comparison of Model Results with Experimental Data

The growth of ice is related to the density, thermal properties and air temperature according to equation (5). From equations (6)–(8), we can see that ρ , k_i , and L are dependent on the ice temperature T_i which generally assumes a linear profile within the ice layer. In order to simplify the ice growth simulation using (5), we let T_i be the mean of melting temperature T_m (at the interface of ice and saline water) and the air-ice interface temperature T_s . The surface temperature T_s is determined from the balance of the net heat flux at the surface [23],

$$T_s = \frac{k_i T_m + c T_a}{\frac{k_i}{h} + c} \quad (11)$$

Since k_i is an implicit function of T_s , equation (11) is solved using an iterative technique. The required salinity information at each growth stage is obtained from equation (9). A finite difference scheme is employed in solving (5), a best-fit value of $c = 8.5\text{ W/m}^2/\text{ }^\circ\text{C}$ has been used. The simulated thin saline ice growth, as indicated by the continuous curve in Figure 1, agrees with the measured ground truth.

In Figures 3 and 4, we also present the comparison between model simulations and the radar measurements with different incident angles for the whole period of ice growth. The dielectric properties of the ice medium used in theoretical simulations include the background ice permittivity with a typical value $\epsilon_1 = (3.15 \pm 0.002)\epsilon_0$, the saline water permittivity calculated from the equation given by Klein and Swift [27], and the brine permittivity determined from the empirical formulas given by Stogryn and Desargant [28]. Other parameters like ice thickness is from equation (5) with the thermal parameters as given in Section III. A. The fractional volume of brine inclusions is calculated based on Cox and Weeks [26], which is

related with the ice temperature and salinity. The salinity is computed from equation (9). For the size and shape of brine inclusions, we assume a value with $b = c$ and $c/a = 3.5$. The assumption of uniform shape is based on the observation of the approximately constant ratio between the co- and cross-polarization returns as illustrated in experimental measurements. A linear size growth with an initial value $a = 0.012$ cm and size expansion factor $g_s = 0.00185$ arcused (1. The good agreement between simulation and measured data also shows the validity for this two-layer saline ice model.

IV. INVERSION ALGORITHM USING SEQUENTIAL MEASUREMENTS

For the growth of saline ice considered in this study, the ice system follows the set of equations (5), (9) and (10), such that the state of ice at a certain stage can be estimated from previous states. With electromagnetic measurements made in a time series, it is helpful to use these correlations to improve the retrieval of relevant physical parameters.

The radiative transfer scattering model described in the previous section provides a relationship between the expected backscatter measurements to the radar parameters and the saline ice characteristics. Let this relationship be expressed as

$$\bar{\sigma}_i = P(t_i, \bar{z}, \bar{x}) + \bar{e}_i \quad (12)$$

where $\bar{\sigma}_i$ is the measurement data vector WIOSC elements consist of backscattering coefficients, $P(t_i, \bar{z}, \bar{x})$ is the model response, and \bar{e}_i represents the discrepancy between the observation and the model result. The index i is used to denote the measurement time at t_i . The array \bar{z} denotes the set of known radar parameters such as the frequency, polarization, and looking direction. The vector \bar{x} contains the pertinent model parameters of saline ice:

$$\bar{x} = [h_0, S_{i0}, d_s, a_0, g_s, c] \quad (13)$$

here $h_0 (= h(t_0))$ is the ice layer thickness at time t_0 at which the reference time for the first set of data taken. The other parameters S_{i0} , d_s , a_0 , g_s , and c have been defined in Section III.B.

In the retrieval analysis, model parameters \bar{x} are to be determined. A common approach to the estimation of parameters is to measure the data $\bar{\sigma}$ and inverse the relation (12), i.e. express the parameter x_j in terms of $\bar{\sigma}$. In principle, the accuracy of the estimation is dependent on the accuracy of model and measurements. A least-square optimization approach is applied in this paper to study the inversion problem of saline ice. The minimization of the sum of squares of the difference between the measured data and the model response is performed by using the Levenberg-Marquardt algorithm [29-31]. The inversion algorithm

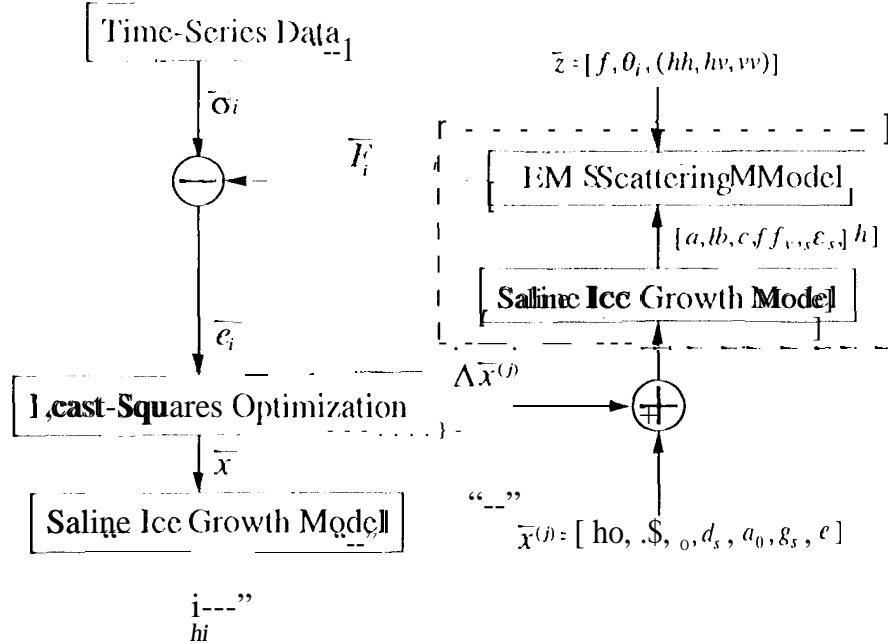


Figure 6: Block diagram of the inversion algorithm with time series measured data.

using time-series measurements is summarized in Figure 6. At the j -th iterative step, the estimated parameters $\bar{x}^{(j)}$ consists of ice parameters at a specific time including the initial ice thickness, initial salinity, initial brine size, desalination factor, brine size growth factor, and the heat transfer coefficient. The subsequent thicknesses, salinity, and brine sizes at different growth stages are calculated according to the saline ice growth model described in Section III.B and the elapsed time between each measurements. This set of ice parameters is then substituted into the electromagnetic scattering model which solves the radiative transfer equation and generates a simulated time-series of backscatters which are compared with the real measurements. Thus, the object function contains the whole time-series measured and model data, in contrast to the results at one specific time. If the predicted results do not match with measured data, the guessed model parameters are to be adjusted. In order to minimize the least-squares object function, the entire series of simulation and experimental results must be matched. In this way, the range of possible retrieved thickness from an initial trial thickness can be reduced and the retrieval may be more robust to the discrepancy between model responses and measurements. The procedure is then repeated until the error threshold is reached. The inverted initial thickness is finally applied back to equation (5) to reconstruct the ice thickness for the whole growth stage.

V. INVERSION RESULTS AND DISCUSSION

The sets of sequentially measured radar data shown in Figures 3 and 4 are applied to

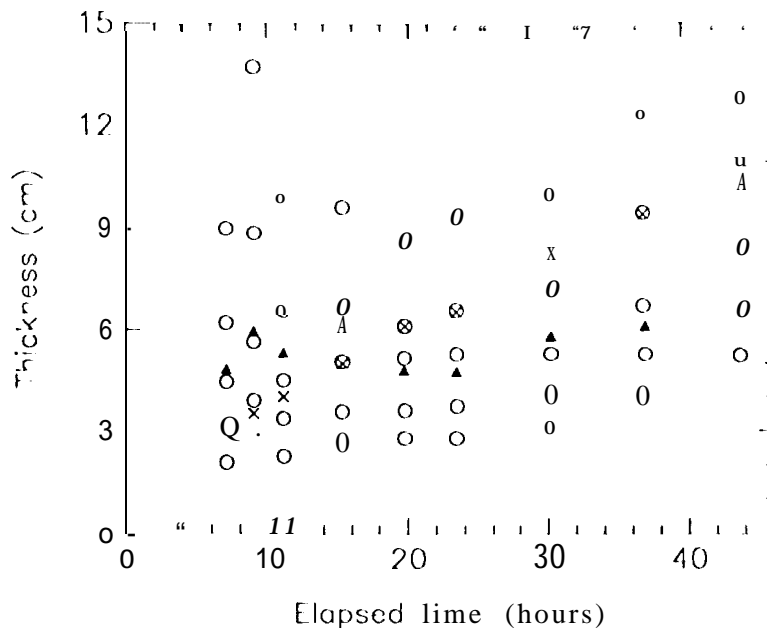


Figure 7: Thickness retrieval without time series information. The circle shows possible combinations of thickness, brine size, and brine volume which may give similar backscattering coefficients at a specific time. Filled triangle represents inversion results with one unknown and without time series information. The ground truth of ice thickness is represented in (10).

the inversion algorithm developed in the previous section. We first consider the thickness retrieval without incorporating the time-series information. For this case, each 25° incident angle data set at a specific time is inverted separately. The open circles shown in Figure 7 indicate the possible solutions of thickness corresponding to the backscatter at that specific time, while the cross symbols represent the measured thickness. This is as expected, since different combinations of thickness, brine volume, and brine size may give a similar backscattering coefficient. In other words, the electromagnetic scattering model only does not provide sufficient information to reconstruct the ice thickness uniquely. We further let thickness be the only unknown model parameters and assume salinity and brine size to have their values the same as those used in Section 11.1. C. The same set of backscatter data at 25° incident angle is applied to invert ice thickness. The retrieved thickness, as denoted by the filled triangles in Figure 7, still shows a large fluctuation from the measured data. The reason is that, as shown in Figure 3, although the radiative transfer model results follow the trend of measured data for the whole ice growth stage, the peak deviations between them can still be as large as 2 dB which may be caused by some measurement uncertainties and the inaccuracy of simplified saline ice scattering model. This example demonstrates an unsuccessful inversion even with only thickness being the unknown parameter.

To circumvent the non-uniqueness and noise problems, the inversion with time-series

model parameters	initial	lower	upper	final value	
	guess	limit	limit	25°	30°
h_0 (cm)	1.0	1.0	8.0	2.87	3.58
a_0 (cm)	0.012	0.012	0.015	0.0128	0.0121
g_s	0.002	0.0015	0.002	0.00169	0.00163
S_{i0} (°/00)	20.0	15.0	20.0	15.55	15.08
d_s (°/00/cm)	0.5	0.5	0.8	0.5	0.54
c (W/m ² /°C)	10.0	8.0	12.0	8.0	8.0

Table 1: Initial guesses, constraints, and inverted model parameters.

measured data is considered next. The initial thickness is a pertinent parameter to be inverted. Since the growth rate of ice is not *a priori* information, the heat transfer coefficient c is also included as an unknown model parameter. Instead of letting all parameters changed freely, which will make the inversion algorithm to be inefficient as well as susceptible to some local minimum attractions or divergence, we set unknown model parameters to be constrained within some physical ranges. Table 1 gives the initial guesses, constraints, and the inverted values of model parameters for this inversion. The reconstructed ice thicknesses are shown in Figures 8 and 9 for two different incident angles 2.5° and 30°, respectively. It is noted that the retrieved ice thickness agrees very well with the measured ice growth by using this time-series inversion algorithm. The retrieved thickness for the 25° data set looks better than the one for 30° which may be due to the larger deviation between model simulation and measured data in cross-polarization at 30° incident angle.

The above cases use the full set of radar measurements with multi-polarization to perform the thickness retrieval. In view of the present available remote sensing sensors with either VV polarization (ERS) or HH polarization (RADARSAT) only, we further apply this algorithm to retrieve ice thickness by using single polarization time-series data. The unknown parameters and limits are the same as the above polarimetric case. Table 2 lists the final inverted results of these parameters. Figures 10 and 11 illustrate the respective inversion results using either HH or VV polarization data at 25° and 30° incident angles. In general, the retrieved ice thickness still shows reasonable agreement with the measured ground truth.

VI. SUMMARY

In this paper, we have developed an inversion algorithm for the thickness of thin saline ice based on the radiative transfer theory, ice growth physics, and parametric estimation method. Time-series measured data are used instead of multi-frequency or multi-angle

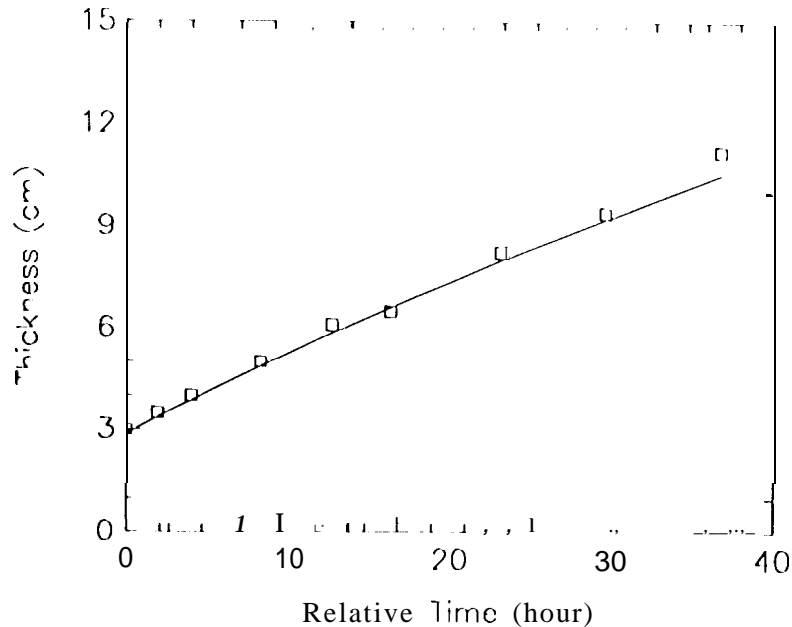


Figure 8: Thickness retrieval with polarimetric time-series data. \square is the measured ice thickness. Solid line represents thickness retrieval with six unknowns and with time series data. Incident angle is 25° .

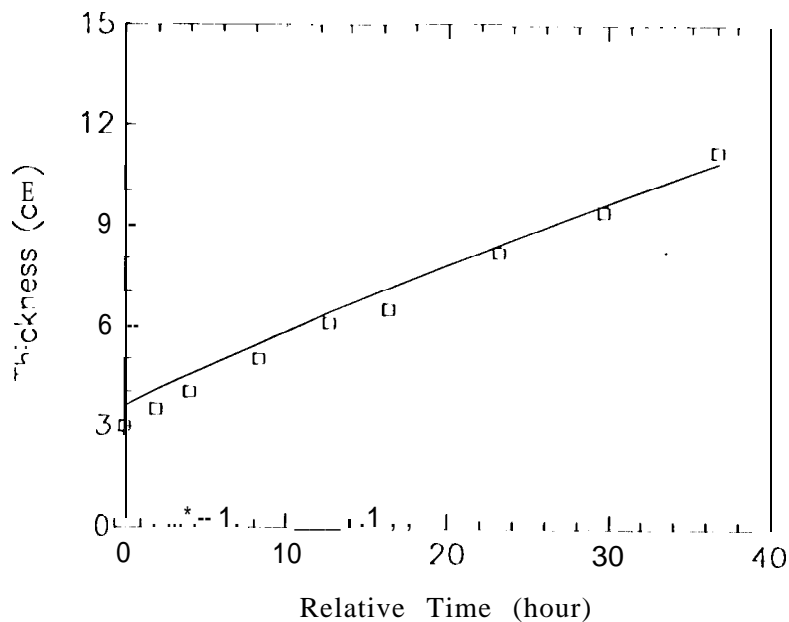


Figure 9: Thickness retrieval with polarimetric time-series data. \square is the measured ice thickness. Solid line represents thickness retrieval with six unknowns and with time series data. Incident angle is 30° .

Parameters	25°	25°	30°	30°
11001 (1)	1111	VV	1111	VV
h_0 (cm)	2.79	4.31	2.39	3.33
a_0 (°/III)	0.012	0.0127	0.012	0.0128
g_s	0.00176	0.00160	0.00178	0.00173
S_{i0} (0/00)	15.0	15.0	15.0	18.1
d_s (°/00/cm)	0.611	0.5	0.5	0.789
c (W/m ² /°C)	8.0	8.0	8.0	9.19

Table 2: Final inverted values of model parameters for different incident angles and different polarizations.

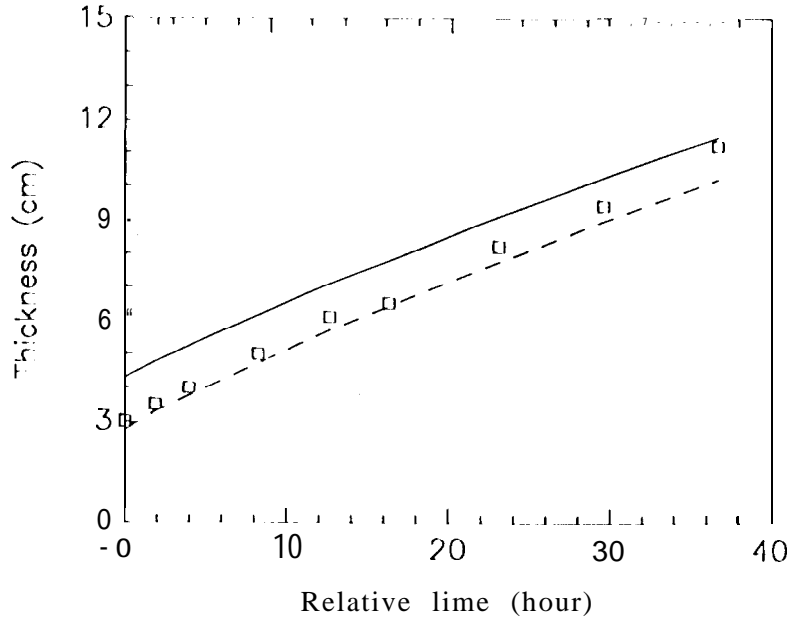


Figure 10: Thickness retrieval with single polarization tilt-series data. \square is the measured ice thickness. Solid line represents thickness retrieval using VV polarization tilt-series data, and dashed line is the result using IIII polarization tilt-series data. Incident angle is 25°.

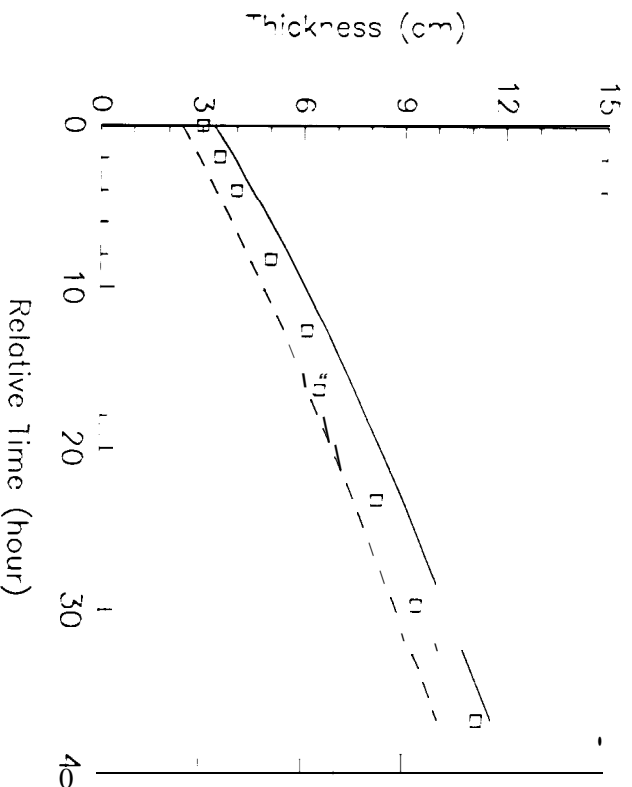


Figure 11: Thickness retrieval with single polarization time-series data. \square is the measured ice thickness. Solid line represents thickness retrieval using VV polarization time-series data, and dashed line is the result using HH polarization time-series data. Incident angle is 30° .

data to reduce the effects of uncertainty and noise. The saline ice growth model provides more information to constrain the parameters. Since the ice growth rate is a function of thickness, different guesses of the initial thickness will produce different growth conditions in the subsequent growth stages and the backscatter response will be affected concomitantly. In order to minimize the least-squares objective function, the entire time-series simulation results must match the whole time-series measurements. Therefore, the range of possible retrieved thicknesses from an initial trial thickness is reduced and the retrieval also becomes more robust to noise at individual data points. As a result, a better retrieval of thickness is achieved by utilizing these time-series measurements in this method. The demonstrated accurate thickness retrieval, as shown in Section V, suggests the potential usage of this algorithm for satellite remote sensing of sea ice.

ACKNOWLEDGMENT

The research in this paper was partially supported by the Office of Naval Research Contract No. : N00014-92-J-4098. The research performed by the Center for Space Microelectronics Technology, Jet Propulsion Laboratory, California Institute of Technology was supported by the Office of Naval Research through an agreement with the National Aeronautics and Space Administration.

APPENDIX

The matrices $\bar{M}(\theta, \phi)$, $\bar{N}(\theta, \phi)$, $\bar{I}(\theta, \phi)$, and the vectors $\bar{S}_1(\theta, \phi)$, $\bar{S}_2(\theta, \phi)$, $\bar{S}_3(\pi - \theta, \phi)$, $\bar{S}_4(\pi - \theta, \phi)$ used in the first-order solution of the radiative transfer equation are given here:

$$\bar{M}(\theta, \phi) = \bar{I}(\theta, \phi) \cdot \bar{D}(\bar{\beta}(\theta, \phi) \sec \theta h) \cdot \bar{I}^{-1}(\theta, \phi) \quad (\text{A.1})$$

$$\bar{N}(\theta, \phi) = \bar{I}(\pi - \theta, \phi) \bar{D}(\bar{\beta}(\pi - \theta, \phi) \sec \theta h) \cdot \bar{I}^{-1}(\pi - \theta, \phi) \quad (\text{A.2})$$

In the equations (A.1) and A.2, the diagonal matrix \bar{D} is

$$\bar{I} \cdot \bar{\beta}(\theta, \phi) \sec \theta h = \begin{array}{c} \left| \begin{array}{cccc} e^{-\beta_1(\theta, \phi) \sec \theta h} & 0 & 0 & 0 \\ 0 & e^{-\beta_2(\theta, \phi) \sec \theta h} & 0 & 0 \\ 0 & 0 & e^{-\beta_3(\theta, \phi) \sec \theta h} & 0 \\ 0 & 0 & 0 & e^{-\beta_4(\theta, \phi) \sec \theta h} \end{array} \right| \quad (\text{A.3}) \end{array}$$

where $\beta_n(\theta, \phi)$ is the eigenvalue of the zeroth-order solution of radiative transfer equation, and their associated eigenvectors form the matrix $\bar{I}(\theta, \phi)$. For an azimuthally symmetric medium, the eigenmatrix can be simplified as

$$\bar{I} = \begin{bmatrix} 1 & 0 & 0 & 0 \\ 0 & 1 & 0 & 0 \\ 0 & 0 & 1 & 1 \\ 0 & 0 & i & -i \end{bmatrix} \quad (\text{A.4})$$

The vectors \bar{S}_1 , \bar{S}_2 , \bar{S}_3 , and \bar{S}_4 are

$$\begin{aligned} \bar{S}(\theta, \phi)_{\alpha} = & \sum_{j=1}^4 \sum_{k=1}^4 \sum_{l=1}^4 \left[\sec \theta \bar{I}^i(\theta, \phi) \right]_{\alpha j} \\ & \cdot \left[\begin{array}{c} 1 - e^{-\beta_k(\pi - \theta_{1i}, \phi_{1i}) \sec \theta_{1i} h} \quad \beta_j(\theta, \phi) \sec \theta h \\ \beta_j(\theta, \phi) \sec \theta + \beta_k(\pi - \theta_{1i}, \phi_{1i}) \sec \theta_{1i} \end{array} \right]_{jk} \\ & \cdot \left[\bar{I}^{-1}(\theta, \phi) \cdot \bar{I}(\theta, \phi; \pi - \theta_{1i}, \phi_{1i}) \cdot \bar{I}(\pi - \theta_{1i}, \phi_{1i}) \right]_{jk} \\ & \cdot \left[\bar{I}^{-1}(\pi - \theta_{1i}, \phi_{1i}) \quad \bar{G}(\theta_{1i}, \phi_{1i}) \cdot \bar{I}^{-1}_{01}(\theta_{0i}) \right]_{kl} \\ & \cdot \left[T_{0i} \right]_l \cdot \begin{array}{c} c_0 \cos \theta_{0i} \\ c_l \cos \theta_{1i} \end{array} \end{aligned} \quad (\text{A.5})$$

$$\begin{aligned}
[S_2(\theta, \phi)]_\alpha &= \sum_{j=1}^4 \sum_{k=1}^4 \sum_{l=1}^4 [\sec \theta \bar{E}(\theta, \phi)]_{\alpha j} \\
&\cdot \left[\begin{array}{c} e^{-\beta_k(\theta_{1i}, \phi_{1i}) \sec \theta_{1i} h} - e^{-\beta_j(\theta, \phi) \sec \theta h} \\ \beta_j(\theta, \phi) \sec \theta - \beta_k(\theta_{1i}, \phi_{1i}) \sec \theta_{1i} \end{array} \right]_{jk} \\
&\cdot \left[\bar{E}^{-1}(\theta, \phi) \cdot \bar{P}(\theta, \phi; \theta_{1i}, \phi_{1i}) \cdot \bar{E}(\theta_{1i}, \phi_{1i}) \right]_{jk} \\
&\cdot \left[\bar{E}^{-1}(\theta_{1i}, \phi_{1i}) \cdot \bar{P}(\theta_{1i}, \phi_{1i}) \cdot \bar{R}_{12}(\theta_{1i}) \cdot \bar{N}(\theta_{1i}, \phi_{1i}) \cdot \bar{T}_{01}(\theta_{0i}) \right]_{kl} \\
&\cdot [\bar{I}_{0i}]_l \cdot \frac{\epsilon_0 \cos \theta_{0i}}{\epsilon'_1 \cos \theta_{1i}} \tag{A.6}
\end{aligned}$$

$$\begin{aligned}
[S_3(\pi - \theta, \phi)]_\alpha &= \sum_{j=1}^4 \sum_{k=1}^4 \sum_{l=1}^4 [\sec \theta \bar{E}(\pi - \theta, \phi)]_{\alpha j} \\
&\cdot \left[\begin{array}{c} e^{-\beta_k(\pi - \theta_{1i}, \phi_{1i}) \sec \theta_{1i} h} - e^{-\beta_j(\pi - \theta, \phi) \sec \theta h} \\ \beta_j(\pi - \theta, \phi) \sec \theta - \beta_k(\pi - \theta_{1i}, \phi_{1i}) \sec \theta_{1i} \end{array} \right]_{jk} \\
&\cdot \left[\bar{E}^{-1}(\pi - \theta, \phi) \cdot \bar{P}(\pi - \theta, \phi; \pi - \theta_{1i}, \phi_{1i}) \cdot \bar{E}(\pi - \theta_{1i}, \phi_{1i}) \right]_{jk} \\
&\cdot \left[\bar{E}^{-1}(\pi - \theta_{1i}, \phi_{1i}) \cdot \bar{G}(\theta_{1i}, \phi_{1i}) \cdot \bar{T}_{01}(\theta_{0i}) \right]_{kl} \\
&\cdot [\bar{I}_{0i}]_l \cdot \frac{\epsilon_0 \cos \theta_{0i}}{\epsilon'_1 \cos \theta_{1i}} \tag{A.7}
\end{aligned}$$

$$\begin{aligned}
[S_4(\pi - \theta, \phi)]_\alpha &= \sum_{j=1}^4 \sum_{k=1}^4 \sum_{l=1}^4 [\sec \theta \bar{E}(\pi - \theta, \phi)]_{\alpha j} \\
&\cdot \left[\begin{array}{c} 1 - e^{-\beta_k(\theta_{1i}, \phi_{1i}) \sec \theta_{1i} h} - \beta_j(\pi - \theta, \phi) \sec \theta h \\ \beta_j(\pi - \theta, \phi) \sec \theta + \beta_k(\theta_{1i}, \phi_{1i}) \sec \theta_{1i} \end{array} \right]_{jk} \\
&\cdot \left[\bar{E}^{-1}(\pi - \theta, \phi) \cdot \bar{P}(\pi - \theta, \phi; \theta_{1i}, \phi_{1i}) \cdot \bar{E}(\theta_{1i}, \phi_{1i}) \right]_{jk} \\
&\cdot \left[\bar{E}^{-1}(\theta_{1i}, \phi_{1i}) \cdot \bar{P}(\theta_{1i}, \phi_{1i}) \cdot \bar{R}_{12}(\theta_{1i}) \cdot \bar{N}(\theta_{1i}, \phi_{1i}) \cdot \bar{T}_{01}(\theta_{0i}) \right]_{kl} \\
&\cdot [\bar{I}_{0i}]_l \cdot \frac{\epsilon_0 \cos \theta_{0i}}{\epsilon'_1 \cos \theta_{1i}} \tag{A.8}
\end{aligned}$$

where α represents the α -th component of the vector, (θ_{1i}, ϕ_{1i}) is the incident direction inside the sea ice layer (region 1), and ϵ'_1 represents the real part of the permittivity ϵ_1 . The matrices \bar{P} and \bar{G} are

$$\bar{P}(\theta, \phi) = \left[\bar{I} - \bar{R}_{12}(\theta) \cdot \bar{N}(\theta, \phi) \cdot \bar{R}_{10}(\theta) \cdot \bar{M}(\theta, \phi) \right]^{-1} \tag{A.9}$$

$$\bar{G}(\theta, \phi) = \left[\bar{I} - \mathbf{k}(\mathbf{u}) \cdot \bar{M}(\theta, \phi) \cdot \bar{R}_{12}(\theta) \cdot \bar{N}(\theta, \phi) \right]^{-1} \tag{A.10}$$

REFERENCES

- [1] w. R. Peltier, *Ice in the Climate System*, New York: Springer-Verlag, 1993.
- [2] G. A. Maykut, "Energy exchange over young sea ice in the central Arctic .," *J. Geophys. Res.*, vol. 83, no. C7, pp. 3646-3658, 1978.
- [3] R. Kwok, E. Rignot, B. Holt, and R. Onstott, "Identification of sea ice types in space-borne synthetic aperture radar data," *J. Geophys. Res.*, vol. 97, no. C2, pp. 2391-2402, 1992.
- [4] ESA, *The ERS-1 System*, European Space Agency Publication, ESA SP-1146, 1992.
- [5] F. D. Carsey, *Science Requirements for RADARSAT/ERS-2 Modifications for the Alaska SAR Facility*, JPL D-1 0443, Jet Propulsion Laboratory, Pasadena, 1993.
- [6] R. Kwok, S. V. Nghiem, S. H. Yuch, and D. D. Huynh, "Retrieval of thin ice thickness from multifrequency polarimetric SAR data," *Remote Sens. Environ.*, vol. 51, no. 3, pp. 361-374, 1995.
- [7] D. Winebrenner, L. D. Farmer, and I. R. Joughin, "On the response of polarimetric synthetic aperture radar signatures at 24-cm wavelength to sea ice thickness in Arctic leads," *Radio Sci.*, vol. 30, no. 2, pp. 373-402, 1995.
- [8] F. J. Ulaby, R. K. Moore, and A. K. Fung, *Microwave Remote Sensing*, Reading, MA: Addison-Wesley, 1982.
- [9] L. Tsang, J. A. Kong, and R. T. Shin, *Theory of Microwave Remote Sensing*, New York: Wiley-Interscience, 1985.
- [10] D. Winebrenner, J. Bredow, A. K. Fung, M. R. Drinkwater, S. Nghiem, A. J. Gow, D. K. Perovich, J. C. Grenfell, H. C. Han, J. A. Kong, J. K. Lee, S. Mudaliar, R. G. Onstott, L. Tsang, and R. D. West, "Microwave sea ice signature modeling," *Microwave Remote Sensing of Sea Ice, Geophys. Monogr. Ser.*, Chapter 8, F. D. Carsey, ed., DC: American Geophysical Union, 1992.
- [11] A. K. Fung, *Microwave Scattering and Emission Models and Their Applications*, Boston: Artech House, 1994.
- [12] S. V. Nghiem, R. Kwok, S. H. Yuch, and M. R. Drinkwater, "Polarimetric signature of sea ice, 1. theoretical model," *J. Geophys. Res.*, vol. 100, no. C7, pp. 13665-13679, 1995.

- [13] A. K. Jordan and M. E. Veysoğlu, "Electromagnetic remote sensing of sea ice," *Inverse Problems*, vol. 10, pp.1041-1058, 1994
- [14] M. E. Veysoğlu, "Direct and inverse scattering models for random media and rough surfaces," *Ph.D. Thesis*, Department of Electrical Engineering and Computer Science, Massachusetts Institute of Technology, 1994.
- [15] M. E. Veysoğlu, H. T. Ewe, A. K. Jordan, R. T. Shin, and J. A. Kong, "Inversion algorithms for remote sensing of sea ice," *Proc. IGARSS'94 Conf.*, pp. 626-628, 1994.
- [16] S. Carslaw and J. C. Jaeger *Conduction of Heat in Solids*, London: Oxford University Press, 1959.
- [17] S. V. Nghiem, R. Kwok, S. H. Yuch, A. J. Gow, D. K. Perovich, J. A. Kong, and G. C. Hsu, "Evolution in polarimetric signatures of thin saline ice under constant growth," submitted for publication.
- [18] M. Wakatsuchi and N. Ono, "Measurements of salinity and volume of brine excluded from growing sea ice," *J. Geophys. Res.*, vol. 88, no. C5, pp. 2943-2951, 1983.
- [19] G. F. N. Cox and W. F. Weeks "Salinity variations in sea ice," *J. Glaciol.*, vol 13, pp. 109-120, ~~94~~
- [20] G. A. Maykut, "The surface heat and mass balance," *The Geophysics of Sea Ice*, Chapter 5, pp.395-463, N. Untersteiner ed., New York: Plenum Press, 1986.
- [21] G. F. N. Cox and W. F. Weeks, "Numerical simulations of the profile properties of undeformed first-year sea ice during the growth season," *J. Geophys. Res.*, vol. 93, pp. 12449-12460, 1988.
- [22] D. A. Meese, "The chemical and structural properties of sea ice in the southern Beaufort Sea," *CRREL Rep. 89-25*, US Army Corps of Eng., Cold Regions Research and Engineering Lab., 1989.
- [23] G. M. Adams, Jr., D. N. French, and W. D. Kingery, "Solidification of sea ice," *Glaciol.*, vol. 3, pp.745-761, 1960.
- [24] G. D. Ashton, "Thin ice growth," *Water Resour Res.*, vol 25, no. 3, pp.564-566, 1989.
- [25] S. Fukusako, "Thermophysical properties of ice, snow, and sea ice," *Int. J. Thermophys.*, vol. 11, no. 2, pp. 353-372, 1990.

- [26] G. F. N. Cox and W. F. Weeks, "Equations for determining the gas and brine volumes in sea-ice samples," *J. Glaciol.*, vol. 29, no. 12, pp. 306-316, 1983.
- [27] L. A. Klein and C. Swift, "An improved model for the dielectric constant of sea water at microwave frequencies," *IEEE Trans. Antennas Propagat.*, vol. AP-25, no. 1, pp. 104-111, 1977.
- [28] A. Stogryn and G. J. Desargant, "The dielectric properties of brine in sea ice at microwave frequencies," *IEEE Trans. Antennas Propagat.*, vol. AP-33, no. 5, pp. 523-532, 1985.
- [29] J. E. Dennis and R. B. Schnabel, *Numerical Methods for Unconstrained Optimization and Nonlinear Equations*, Englewood Cliffs, NJ: Prentice-Hall, 1983.
- [30] D. W. Marquardt, "An algorithm for least-squares estimation of nonlinear parameters," *J. Soc. Indust. Appl. Math.*, vol. 11, pp. 431-441, 1963.
- [31] J. J. Kuester and J. H. Mize, *Optimization Techniques with Fortran*, New York: McGraw-Hill, 1973.